

The DESI PRObabilistic Value-Added Bright Galaxy Survey (PROVA-BGS) Mock Challenge

CHANGHOON HAHN,¹ GYUBIN KWON, MALGORZATA SIUDEK, RITA TOJEIRO, AND GQP WG

¹*Department of Astrophysical Sciences, Princeton University, Peyton Hall, Princeton NJ 08544, USA*

ABSTRACT

In this project, we present the methodology for inferring physical properties of galaxies from joint SED fitting of the DESI optical photometry and spectroscopy. We construct realistic forward modeled DESI data from star formation and chemical enrichment histories of galaxies in the L-GALAXIES semi-analytic model and the ILLUSTRIS TNG hydrodynamic simulations. Then, using these mock observations, we demonstrate that the stellar mass and SFR posteriors from our SED fitting are consistent with constraints from other SED fitting methods in the literature and, more importantly, the input stellar masses and SFRs from the simulations. The SED fitting we present and validate in this project will be used to construct the PRObabilistic Value-Added Bright Galaxy Survey (PROVABGS) from DESI observations.

Keywords: keyword1 – keyword2 – keyword3

1. INTRODUCTION

Large galaxy surveys have been transformational for our understanding of galaxy evolution. With surveys such as the Sloan Digital Sky Survey (SDSS [York et al. 2000](#)), Galaxy and Mass Assembly survey (GAMA [Driver et al. 2011](#)), and PRISM Multi-object Survey (PRIMUS [Coil et al. 2011](#)), we have now established the global trends of galaxies in the local universe.

The Dark Energy Spectroscopic Instrument (DESI) marks the next stage in large galaxy surveys. Over the next five years, DESI will use its 5000 robotically-actuated fibers to provide redshifts of ~ 30 million galaxies over $\sim 14,000$ deg², a third of the sky ([Collaboration et al. 2016a](#)). The redshifts will be spectroscopically measured from optical spectra that spans the wavelength range $3600 < \lambda < 9800\text{\AA}$ with spectral resolutions $R = \lambda/\Delta\lambda = 2000 - 5000$. In addition, DESI targets will also have photometry from the Legacy Imaging Surveys Data Release 9 (LS [Dey et al. 2019](#)), used for target selection. LS is a combination of three public projects (Dark Energy Camera Legacy Survey, Beijing-Arizona Sky Survey, and Mayall z -band Legacy Survey) that jointly imaged the DESI footprint in three optical bands (g , r , and z). It also includes photometry in the WISE $W1$, $W2$, $W3$, and $W4$ infrared bands. **The infrared photometry is from all imaging through year 4 of NEOWISE-**

TODO

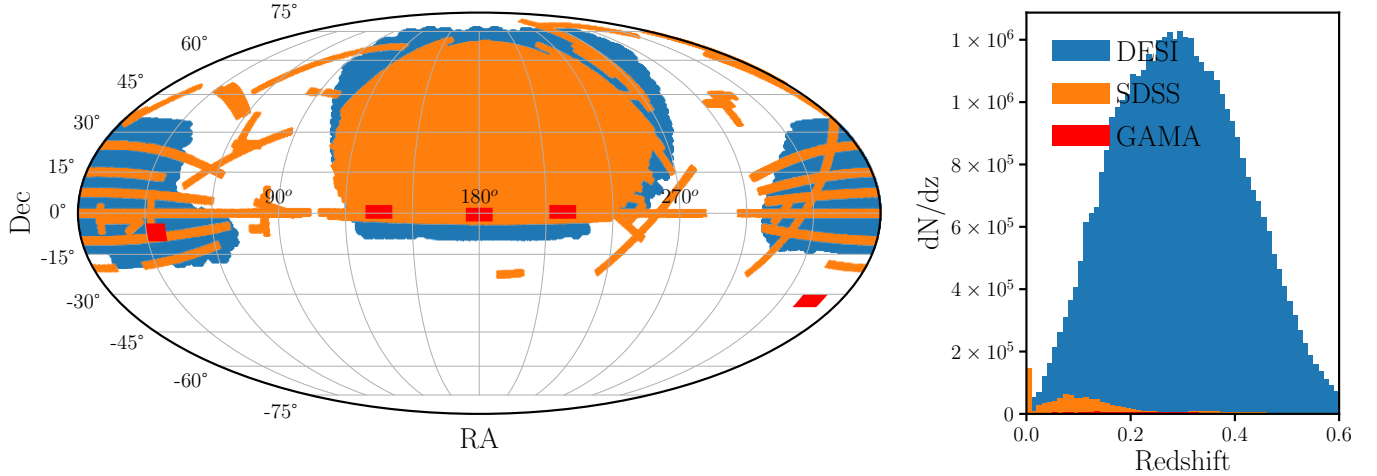


Figure 1. DESI will conduct the largest spectroscopic survey to date covering $\sim 14,000 \text{ deg}^2$. During dark time, DESI will measure >20 million spectra of luminous red galaxies, emission line galaxies, and quasars out to $z > 3$. During bright time, DESI will measure the spectra of ~ 10 million galaxies out to $z \sim 0.4$ with the Bright Galaxy Survey (BGS). *Left:* With its $\sim 14,000 \text{ deg}^2$ footprint (black), DESI will cover $\sim 2\times$ the SDSS footprint (blue; $\sim 7000 \text{ deg}^2$) and $\sim 45\times$ the GAMA footprint (orange; $\sim 300 \text{ deg}^2$). *Right:* Over this footprint, the BGS will provide spectra for a magnitude limited sample of ~ 10 million galaxies down to $r < 20$, two orders of magnitude deeper than the SDSS main galaxy sample and 0.2 mag deeper than GAMA.

Reactivation force-photometered in the unWISE maps at the locations of LS optical sources (cite).

During bright time (*e.g.* when the moon is above the horizon), DESI will conduct the Bright Galaxy Survey (BGS). BGS will provide a $r < 19.5$ magnitude-limited sample of ~ 10 million galaxies out to redshift $z < 0.6$ — *i.e.* the BGS bright sample. It will also provide a surface brightness and color selected sample of **X faint galaxies with $19.5 < r < 20.1$** . With these BGS galaxy samples we will be able to measure the Baryon Acoustic Oscillation to the cosmic variance limit. They also have the potential to unlock higher-order statistics and multiple-tracer methods. **overview of cosmology impact of BGS** (Collaboration et al. 2016a,b).

BGS will be equally transformative for galaxy evolution. Compared to the seminal SDSS main galaxy survey, BGS will provide optical spectra two magnitudes deeper, over twice the sky, and **X billion years farther**. This provides a unique opportunity to **develop a more complete picture of low mass galaxies**. **Extend detailed galaxy environment studies to higher redshifts**. **Overall more complete picture of galaxy evolution**

Alongside the BGS, the DESI collaboration will also provide a number of Value-Added Catalogs (VAC) with detailed properties of BGS galaxies to maximize the scientific impact of DESI. In the past, such VACs have been instrumental for hundreds of scientific analyses (see ?, for a review). The New York University-Value-Added Galaxy Catalog (NYU-VAGC Blanton et al. 2005), for instance, provided photometric properties such as absolute magnitudes of SDSS galaxies. The MPA-JHU cat-

TODO

TODO

TODO

TODO

alog¹ provided spectral properties such as emission line luminosities ?. Despite being released over a decade ago, these VACs are still widely used today (*e.g.* ?).

One key VAC that DESI will provide is the PRObabilistic Valued-Added Bright Galaxy Survey (PROVABGS) catalog. For all ~ 10 million BGS galaxies, PROVABGS will provide posterior probability distributions of physical properties such as stellar mass (M_*), star formation rate (SFR), metallicity, and stellar age. These properties will be inferred from the LS photometry and DESI spectroscopy using a state-of-the-art Bayesian modeling of the galaxy spectral energy distribution (SED). With these properties, PROVABGS will enable direct extension of previous works to the more complete and statistically powerful spectroscopic galaxy sample. For instance, M_* values will be used to measure the stellar mass function down to $M_* \sim 10^8 M_\odot$ (Hahn *et al.* in prep.). M_* and SFR will also be used to more precisely measure the star forming sequence. Detailed galaxy environment studies will be

TODO

Moreover, instead of point estimates of galaxy properties, PROVABGS will provide full posterior distributions. provabgs introduces a new frontier of low signal-to-noise statistically powerful sample that will require

TODO

TODO

Why do we need a mock challenge? *i.e.* what are the goals of this paper? We want to test and cement our methodology specifically for our GQP analysis before SV data comes out. As part of the survey preparation, we have all the tools to accurately forward model observations. details on some of the specific tools and what we're able to simulate: realistic spectroscopy. realistic photometry. realistic spectro-photometry All of this gives us a rare opportunity to test our methodology on bespoke simulations.

TODO

overview of the paper A mock challenge is also great for testing new methodology. BGS is a bright time survey and will push the boundaries of low SNR spectra. But if we can find a way to infer robust galaxy properties the statistical payout is awesome. Something also about LRGs We're also trying to robustly fit spectra and photometry simultaneously. This has been done before (citations) but not extensively tested on simulations.

TODO

TODO

TODO

2. SIMULATIONS

In this Section, we describe how we construct mock observations for simulated galaxies from the L-GALAXIES semi-analytic galaxy formation model. We use a forward model that includes realistic noise, instrumental effects, and observational systematics and produces DESI-like photometry and spectra. Later, we apply Bayesian SED modeling to these mock observations and demonstrate that we can accurately infer the true galaxy properties.

2.1. *L-Galaxies*

L-GALAXIES (hereafter LGAL; Henriques *et al.* 2015) is a state-of-the-at semi-analytic galaxy formation model run on subhalo merger trees from the Millennium (Springel *et al.* 2005) and Millenium-II (Boylan-Kolchin *et al.* 2009) N -body simulations. Millenium-I and II provide a dynamic range of $10^{7.0} M_\odot < M_* < 10^{12} M_\odot$ and adopts a Collaboration *et al.* (2014) Λ CDM cosmology. LGAL includes

¹ <https://wwwmpa.mpa-garching.mpg.de/SDSS/DR7/>

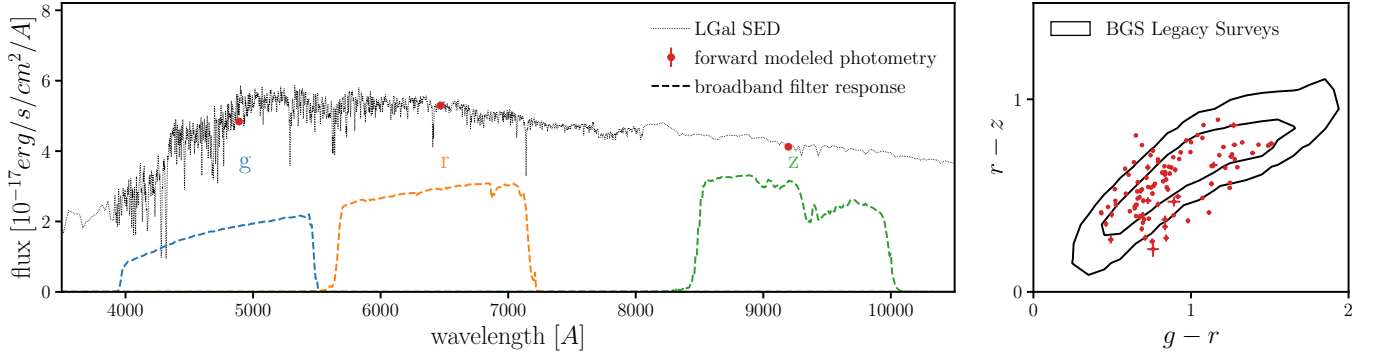


Figure 2. *Left:* We forward model DESI g , r , and z photometry (red) for our simulated galaxies (Section 2.1) by convolving their SEDs (dotted) with their broadband filters (dashed) and then applying an empirical noise model based on BGS objects in LS (Section 2.3). *Right:* The $g - r$ and $r - z$ color distribution of the forward modeled LGAL photometry is in good agreement with the color distribution of LS BGS objects (black contours).

prescriptions for gas infall and cooling, star formation, disc and bulge formation, stellar and black hole feedback, and the environmental effects of tidal and ram-pressure stripping. AGN feedback, which prevents hot gas from cooling, is the major mechanism for quenching star formation in massive galaxies. LGAL model parameters are calibrated against the observed stellar mass functions and passive fractions at four different redshifts from $z = 3$ to 0. For further detail on the LGAL SAM, we refer readers to [Henriques et al. \(2015\)](#).

2.2. Spectral Energy Distributions

For each simulated galaxy, LGAL provides the star formation histories (SFHs) and chemical enrichment histories (ZH) for its bulge and disk components separately, in approximately log-spaced lookback time bins. We treat each lookback time bin, i , as a single stellar population (SSP) of age t_i . Then, we derive the luminosities of the bulge and disk components by summing up the luminosities of all of their SSPs:

$$L^{\text{comp.}}(\lambda) = \sum_i (\text{SFH}_i^{\text{comp.}} \Delta t_i) L_{\text{SSP}}(\lambda; t_i, Z_i^{\text{comp.}}). \quad (1)$$

$\text{SFH}_i^{\text{comp.}}$ and $Z_i^{\text{comp.}}$ are the star formation rate and metallicity of the bulge or disk component in lookback time bin i . Δt_i is the width of the bin. L_{SSP} corresponds to the luminosity of the SSP, which we calculate using the Flexible Stellar Population Synthesis (FSPS [Conroy et al. 2009; Conroy & Gunn 2010](#)) model. For FSPS, we use the MIST isochrones ([Paxton et al. 2011, 2013, 2015; Choi et al. 2016; Dotter 2016](#)), the MILES spectral library ([Sánchez-Blázquez et al. 2006](#)), and the [Chabrier \(2003\)](#) initial mass function (IMF).

Next, we apply velocity dispersions to $L^{\text{comp.}}(\lambda)$. For the disk, we apply a fixed 50 km/s velocity dispersion; for the bulge, we derive its velocity dispersion using the [Zahid et al. \(2016\)](#) empirical relation that depends on the total bulge mass. Then, we apply dust attenuation to stellar emission in the disk component (L^{disk}) based on the cold gas content and orientation of the disk. We derive the attenuation curve using a mixed-screen model with the [Mathis \(1983\)](#) dust extinction curve. Stellar

emission from stars younger than 30Myr are further attenuated with a uniform dust screen and a wavelength dependent optical depth. @rita further details and citations for the mixed-screen model
 No dust attenuation is applied to the bulge component. @rita how come?

TODO
 TODO

Finally, we combine the attenuated disk component and the bulge component to construct the total luminosity of the simulated galaxy and then convert this rest-frame luminosity to observed-frame SED flux using its redshift, z .

$$f_{\text{SED}}(\lambda) = \frac{A(\lambda)L^{\text{disk}}(\lambda) + L^{\text{bulge}}(\lambda)}{4\pi d_L(z)^2(1+z)}. \quad (2)$$

$A(\lambda)$ is the dust attenuation for the disk component described above and $d_L(z)$ is the luminosity distance. In the left panel of Figure 2, we present an example of the SED flux constructed for an arbitrary LGALgalaxy (black).

2.3. Forward Modeling DESI Photometry

In this section, we describe how we construct realistic LS-like photometry from the SEDs of simulated galaxies described in the last section. First, we convolve the SEDs with the broadband filters of the Legacy Survey to generate broadband photometric fluxes:

$$f_X = \int f_{\text{SED}}(\lambda) R_X(\lambda) d\lambda \quad (3)$$

where f_{SED} is the galaxy SED (Eq. 2) and R_X is the transmission for filter X . We generate photometry for the g , r , and z optical bands. Next, we apply realistic measurement uncertainties to the derived photometry using a simple empirical . We match each simulated galaxy to a BGS object from LS DR9 with the nearest r -band magnitude and $g - r$ and $r - z$ color. The photometric uncertainties (σ_X) and r -band fiber flux (f_r^{fiber}) of the BGS object are then assigned to the simulated galaxy. We sample a Gaussian distribution with standard deviation σ_X and apply it to construct realistic LS-like photometry:

$$\hat{f}_X = f_X + n_X \quad \text{where } n_X \sim \mathcal{N}(0, \sigma_X). \quad (4)$$

Finally, we impose the target selection criteria of BGS (Ruiz-Macias et al. 2021, Hahn et al. in prep.). In the left panel of Figure 2, we overplot the forward modeled photometry (red) ontop of the SED flux (black) for an arbitrary LGALgalaxy. For reference, we also plot R_X for the g , r , and z bands of the Legacy Survey in blue, orange, and green respectively. On the right panel, we compare the $g - r$ versus $r - z$ color distribution for the forward modeled LGALgalaxies (red) to the color distribution of BGS objects in LS (black contour). The forward modeled photometry show good agreement with LS BGS objects in color space.

2.4. Forward Modeling DESI Spectra

In this section, we describe how we construct realistic DESI-like spectroscopy from the SEDs of simulated galaxies. Our forward model involves modeling the fiber aperture effect and applying a noise model that accurately reproduces the bright time observations of BGS.

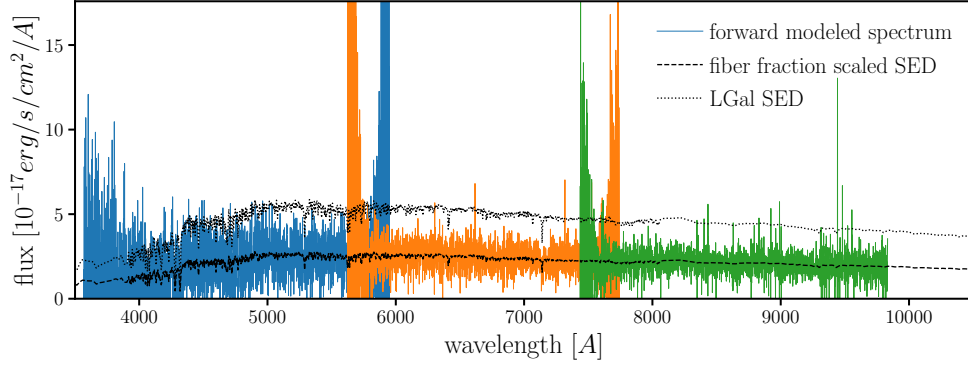


Figure 3. We construct simulated DESI spectra (solid) for LGAL simulated galaxies by applying a fiber aperture correction to the SED (dashed) and a realistic DESI noise model. We apply a fiber aperture correction by scaling down the full SED (dotted) by the r -band fiber fraction derived from the Legacy Surveys imaging. The noise model accounts for the DESI spectrograph response and an atmosphere model that accounts for the bright time observing conditions of BGS. Our forward model produces DESI-like spectra for all three arms of the DESI spectrographs: b , r , and z (blue, orange, and green, respectively). For more details, we refer readers to Section 2.4.

DESI uses fiber-fed spectrographs with fibers that have angular radii of $1''$. Only the light from a galaxy within this fiber aperture is collected by the instrument. LS provides measurements of photometric fiber flux within a $1''$ radius aperture (f_X^{fiber}), which estimates the flux that passed through to the fibers. When we assign photometric uncertainties to our simulated galaxies based on r , $g-r$, and $r-z$ in Section 2.3, we also assign r -band fiber flux. We model the SED flux that passes through the fiber by scaling the SED flux by the r band fiber fraction, the ratio of the r -band fiber flux over the total r band flux:

$$f^{\text{spec}}(\lambda) = \left(\frac{f_r^{\text{fiber}}}{f_r} \right) f_{\text{SED}}(\lambda). \quad (5)$$

This fiber aperture correction assumes that there is no significant color dependence. We also assume that there are no significant biases in the fiber flux measurements in LS due to miscentering of objects.

Do we want to say more about this assumption? Also cite Marta's paper investigating aperture effect. TODO

In addition to using it for the aperture correction, we also use f_r^{fiber} to derive “measured” \hat{f}_r^{fiber} :

$$\hat{f}_r^{\text{fiber}} = f_r^{\text{fiber}} + n_r^{\text{fiber}} \quad \text{where } n_r^{\text{fiber}} \sim \mathcal{N} \left(0, \frac{f_r^{\text{fiber}}}{f_r} \sigma_r \right). \quad (6)$$

We later use \hat{f}_r^{fiber} to set the prior on the nuisance parameter of our SED modeling (Section 3).

Next, we apply a noise model that simulates the DESI instrument response and bright time observing conditions of BGS. We use the spectral simulation pipeline of **cite survey simulations paper and list details**². More specifically, we use nominal dark time observing conditions with 180s exposure time. These conditions accurately reproduce the spectral noise and redshift success rates TODO

² <https://specs.sim.readthedocs.io>

of observed BGS exposures in DESI survey validation data (Hahn *et al.* in prep.). In Figure 2.3, we present the forward modeled BGS spectrum of a LGAL galaxy (solid). For reference, we include the full SED (dotted) and fiber fraction scaled SED (dashed) of the galaxy.

3. JOINT SED MODELING OF PHOTOMETRY AND SPECTRA

3.1. *Stellar Population Synthesis Modeling*

PROVABGS will provide inferred galaxy properties derived from joint SED modeling of DESI photometry and spectra. For the SED modeling, we use a state-of-the-art stellar population synthesis (SPS) model that uses a non-parametric SFH with a star-burst, a non-parametric ZH that varies with time, and a flexible dust attenuation prescription.

The form of the SFH is one of the most important factors in the accuracy of an SPS model. In general, the form of the SFH requires balancing between being flexible enough to describe the wide range of SFHs in observations while not being too flexible that it can describe any SFH at the expense of constraining power. If the model SFH is not flexible enough to describe actual SFHs of galaxies, then unbiased galaxy properties cannot be inferred using the SPS model. For instance, most SPS models (*e.g.* CIGALE, Serra *et al.* 2011; BAGPIPES, Carnall *et al.* 2017) use parametric SFH such as the exponentially declining τ -model. Such functional forms, however, produce biased estimates of galaxy properties (*e.g.* M_* and SFR) when used to fit mock observations of simulated galaxies (Simha *et al.* 2014; ?; Carnall *et al.* 2018). On the other hand, many non-parametric forms of the SFH are overly flexible and allow unphysical SFHs (Leja *et al.* 2019), which unnecessarily increases parameter degeneracies and discards constraining power.

In our SPS model, we use a non-parametric SFH with two components: one based on non-negative matrix factorization (NMF) basis functions and a starburst component. For the first component, SFH is a linear combination of NMF SFH bases:

$$\text{SFH}^{\text{NMF}}(t, t_{\text{age}}) = \sum_{i=1}^4 \beta_i \frac{s_i^{\text{SFH}}(t)}{\int_0^{t_{\text{age}}} s_i^{\text{SFH}}(t) dt}. \quad (7)$$

$\{s_i^{\text{SFH}}\}$ are the NMF basis functions and $\{\beta_i\}$ are the coefficients. The integral in the denominator normalizes the NMF basis functions to unity. We constrain $\sum_i \beta_i = 1$, so the total SFH of the component over the age of the galaxy (t_{age}) is normalized to unity. $\{s_i^{\text{SFH}}\}$ are from Tojeiro *et al.* (in prep.) and derived from the IllustrisTNG cosmological hydrodynamic simulation (Nelson *et al.* 2018; Pillepich *et al.* 2018; Springel *et al.* 2018). The SFHs of simulated galaxies IllustrisTNG are compiled, rebinned, and smoothed more details here. Afterwards, we perform non-negative matrix factorization (Lee & Seung 1999; Cichocki & Phan 2009; Févotte & Idier 2011) on the smooth SFHs to derive $\{s_i^{\text{SFH}}\}$. We find that 4 components is sufficient to accurately reconstruct the SFHs from IllustrisTNG. Assuming that the SFHs of IllustrisTNG galaxies resemble the SFHs of actual observed galaxies, our NMF form provides a compact and flexible representation of the SFHs.

The NMF basis functions are derived from smooth SFHs, which means that it does not include any stochasticity. However, observations and high resolution zoom-in hydrodynamical simulations

TODO

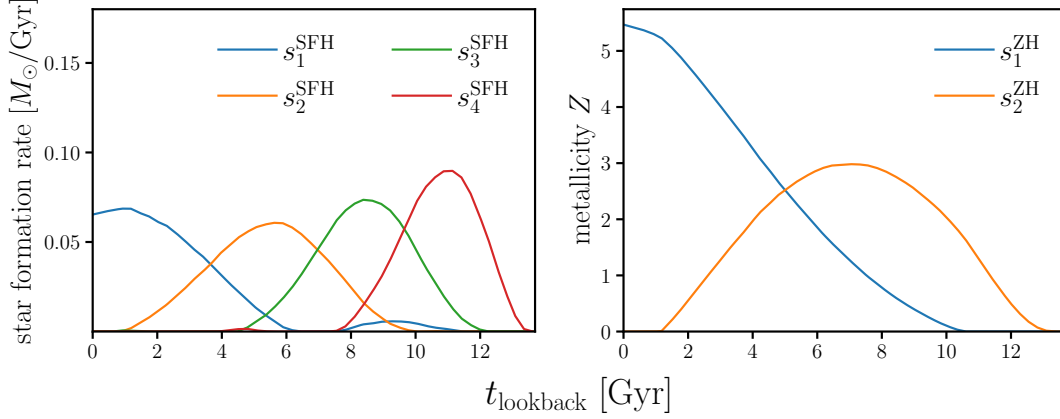


Figure 4. Non-negative matrix factorization basis functions for the SFH (left) and ZH (right). These basis functions are derived from the SFHs and ZHs of simulated galaxies in the IllustrisTNG cosmological hydrodynamic simulations.

both find significant stochasticity in galaxy SFHs (Sparre et al. 2017; Caplar & Tacchella 2019; Hahn et al. 2019; Iyer et al. 2020). To include this stochasticity in our SPS model, we include a starburst component that consists of a SSP in the SFH. For the total SFH, we use

$$\text{SFH}(t, t_{\text{age}}) = (1 - f_{\text{burst}}) \text{SFH}^{\text{NMF}}(t, t_{\text{age}}) + f_{\text{burst}} \delta_{\text{D}}(t - t_{\text{burst}}). \quad (8)$$

f_{burst} is the fraction of total stellar mass formed during the starburst; t_{burst} is the time at which the starburst occurs; δ_{D} is the Dirac delta function. In total we have 6 free parameters in our SFH: 4 NMF basis coefficients (β_i), f_{burst} , and t_{burst} .

Another key part of an SPS model is the ZH, or chemical enrichment history. Current SPS models mostly assume a ZH that does not vary over time (Carnall et al. 2017; Leja et al. 2019). Since galaxies in hydrodynamical simulations and observations do not have constant metallicities throughout their history, this assumption can significantly bias the inferred galaxy properties. Instead, for our ZH, we take a similar approach to the SFH and use NMF basis functions:

$$\text{ZH}(t) = \sum_{i=1}^2 \gamma_i s_i^{\text{ZH}}(t). \quad (9)$$

$\{s_i^{\text{ZH}}(t)\}$ are the ZH NMF basis functions and $\{\gamma_i\}$ are the coefficients. $\{s_i^{\text{ZH}}(t)\}$ are fit using the ZHs of simulated galaxies from IllustrisTNG. We use two NMF components, so our ZH prescription has 2 free parameters.

Next, we use the SFH and ZH above to model the unattenuated rest-frame luminosity as a linear combination of multiple SSPs, evaluated at logarithmically-spaced lookback time bins. We use a fixed log-binning with the bin edges starting with $(0, 10^{6.05}\text{yr})$, $(10^{6.05}, 10^{6.15}\text{yr})$, and continuing on with bins of width 0.1 dex. The binning is truncated at the age of the model galaxy. For a $z = 0$ galaxy, we use 43 t_{lookback} bins. We use log-spaced t_{lookback} bins because it better reproduces galaxy luminosities evaluated with much higher resolution t_{lookback} binning than linearly-spacing, for the same number of

bins. At every t_{lookback} bin i , we evaluate the luminosity of a SSP with $ZH(t_i)$, where t_i is the center of t_{lookback} bin, and total stellar mass calculated by resampling the SFH in Eq. 8. We use FSPSto evaluate the SSP luminosities and use the MIST isochrones, MILES spectral library, and the Chabrier (2003) IMF (same as in Section 2.2). Since we use MIST isochrones, we impose a minimum and maximum limit to ZH based on its coverage: 4.49×10^{-5} and 4.49×10^{-2} , respectively. Our stellar metallicity range is significantly broader than previous studies, *e.g.* Carnall et al. (2017); Leja et al. (2017); Tacchella et al. (2021).

Before we combine the SSP luminosities, we apply dust attenuation. We use a two component Charlot & Fall (2000) dust attenuation model with birth cloud (BC) and diffuse-dust (ISM) components. The BC component represents the extra dust attenuation of young stars that are embedded in molecular clouds and HII regions. For SSPs younger than $t_i < 100\text{Myr}$, we apply the following BC dust attenuation:

$$L_i(\lambda) = L_i^{\text{unatten.}}(\lambda) \exp \left[-\tau_{\text{BC}} \left(\frac{\lambda}{5500\text{\AA}} \right)^{-0.7} \right]. \quad (10)$$

τ_{BC} is the BC optical depth that determines the strength of the BC attenuation. Afterwards, *all* SSPs are attenuated by the diffuse dust using the Kriek & Conroy (2013) attenuation curve parameterization:

$$L_i(\lambda) = L_i^{\text{unatten.}}(\lambda) \exp \left[-\tau_{\text{ISM}} \left(\frac{\lambda}{5500\text{\AA}} \right)^{n_{\text{dust}}} (k_{\text{Cal}}(\lambda) + D(\lambda)) \right]. \quad (11)$$

τ_{ISM} is the diffuse dust optical depth. n_{dust} is the ? dust index, which determines the slope of the attenuation curve. $k_{\text{Cal}}(\lambda)$ is the ? attenuation curve and $D(\lambda)$ is the UV dust bump, parameterized using a Lorentzian-like Drude profile:

$$D(\lambda) = \frac{E_b(\lambda \Delta\lambda)^2}{(\lambda^2 - \lambda_0^2)^2 + (\lambda \Delta\lambda)^2} \quad (12)$$

where $\lambda_0 = 2175\text{\AA}$, $\Delta\lambda = 350\text{\AA}$, and $E_b = ?$ are the central wavelength, full width at half maximum, and strength of the bump, respectively. Once dust attenuation is applied to the SSPs, we sum them up to get the rest-frame luminosity of the galaxy. In total, our SPS model has 12 free parameters: M_* , 4 SFH basis coefficients, f_{burst} , t_{burst} , 2 ZH basis coefficients, τ_{BC} , τ_{ISM} , and n_{dust} .

In practice, evaluating each SSP using FSPS requires X seconds. For each model evaluation, we evaluate ~ 43 SSPs in each of the log-spaced t_{lookback} bins; this takes X seconds. Though this is not a prohibitive computational cost on its own, sampling a high dimensional parameter space for inference requires $> 100,000$ evaluations — *i.e.* > 100 CPU hours *per galaxy*. For the > 10 million BGS galaxies, this would require *a billion* CPU hours. Instead, we use an emulator for the model luminosity, which uses a Principal Component Analysis (PCA) neural network (NN) following the approach of Alsing et al. (2019).

Our emulator consists of a NN and PCA basis functions. The NN provides a flexible and accurate mapping between the SPS model parameters and PCA coefficients — *i.e.* the NN predicts PCA coefficients for a given set of SPS parameters. Then the linear combination of the predicted coefficients and PCA basis functions give us the emulated model luminosity. The PCA basis functions and NN

TODO

TODO

TODO

TODO

TODO

Table 1. Parameters of the PROVABGS SPS model used for joint SED modeling of DESI photometry and spectroscopy.

name	description	prior
$\log M_*$	log galaxy stellar mass	uniform over [8, 13]
$\beta_1, \beta_2, \beta_3, \beta_4$	NMF basis coefficients for SFH	Dirichlet prior
f_{burst}	fraction of total stellar mass formed in starburst event	uniform over [0, 1]
t_{burst}	time of starburst event	uniform over [10Myr, 13.2Gyr]
γ_1, γ_2	NMF basis coefficients for ZH	uniform over []
τ_{BC}	Birth cloud optical depth	uniform over []
τ_{ISM}	diffuse-dust optical depth	uniform over []
n_{dust}	? dust index	uniform over []
f_{fiber}	spectrum fiber-aperture effect normalization	Gaussian []

are trained using 1,000,000 pairs of SPS parameters and model luminosity, $(\theta, L(\lambda; \theta))$. Throughout the wavelength range relevant for BGS, $3000 < \lambda < 9800\text{\AA}$, we achieve $< 1\%$ accurate with the emulator. For details on the training, validation, and performance of our PCA NN emulator, we refer readers to Kwon *et al.* (in prep.).

From the rest-frame luminosity, we obtain the observed-frame, redshifted, flux in the same way as Eq. 2. In our case, redshift is not a free parameter since we will have spectroscopic redshifts for every DESI BGS galaxy. To model DESI photometry, we convolve the model flux with the LS broadband filters as in Eq. 3. To model DESI spectra, we first apply Gaussian velocity dispersion. In this work, we keep velocity dispersion fixed at *0km/s* but in practice velocity dispersion can be set as a free parameter. Then the broadened flux is resampled into the wavelength binning of the observed DESI spectra, which has spectral resolution $R = 2000 - 5000$ over $3600 < \lambda < 9800\text{\AA}$. Since the DESI spectra does not necessarily include all the light of a galaxy, we include a nuisance parameter f_{fiber} , a normalization factor on the spectra to account for fiber aperture effects. Finally, the SPS model photometry and spectrum can be directly compared to observations.

TODO

3.2. Bayesian Parameter Inference

Using the SPS model above, we perform Bayesian parameter inference to derive posterior probability distributions of the SPS parameters from photometry and spectroscopy. From Bayes rule, we write down the posterior as

$$p(\theta | \mathbf{X}) \propto p(\theta) p(\mathbf{X} | \theta) \quad (13)$$

where \mathbf{X} is the photometry or spectrum and θ is the set of SPS parameters. $p(\mathbf{X} | \theta)$ is the likelihood, which we calculate separately for the photometry

$$\mathcal{L}^{\text{photo}} \propto \exp \left[-\frac{1}{2} \left(\frac{X^{\text{photo}} - m^{\text{photo}}(\theta)}{\sigma^{\text{photo}}} \right)^2 \right] \quad (14)$$

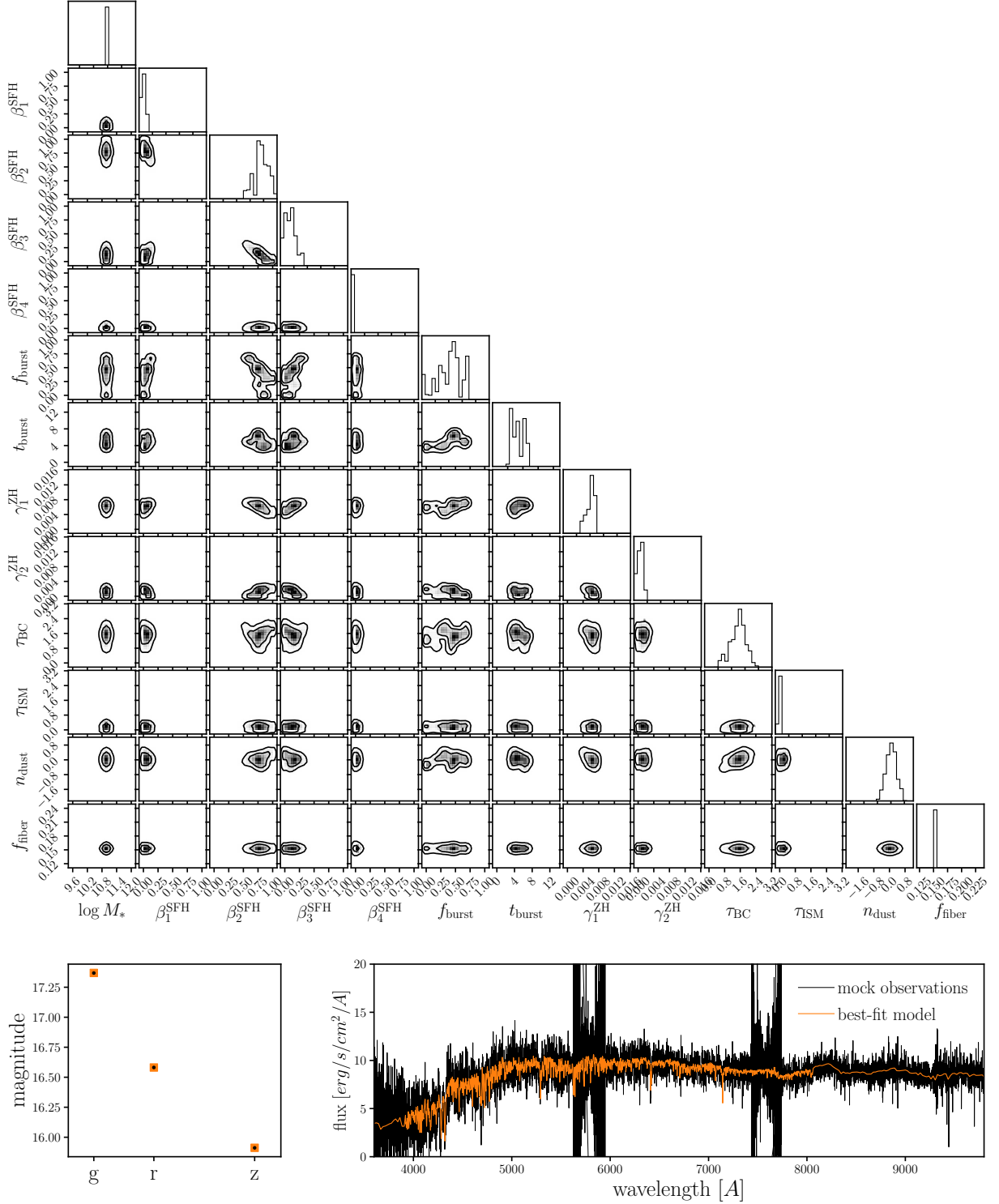


Figure 5. *Top:* Posterior probability distribution of our 12 SPS model parameters derived from joint SED modeling of the mock DESI photometry and spectrum. The contours mark the 68 and 95% percentiles. We use a Gaussian likelihood and the prior specified in Table 3.1 to evaluate the posterior and sample the distribution using ensemble slice MCMC. *With our Bayesian SED modeling approach, we capture the significant parameter degeneracies and multimodality of the posterior distribution.* *Bottom:* We compare the best-fit model observables (orange) to the mock observations (black). We find excellent agreement for both the LS photometry (left) and the DESI spectrum (right).

and for the spectrum

$$\mathcal{L}^{\text{spec}} \propto \exp \left[-\frac{1}{2} \left(\frac{X^{\text{spec}} - m^{\text{spec}}(\theta)}{\sigma^{\text{spec}}} \right)^2 \right]. \quad (15)$$

m^{photo} and m^{spec} represent SPS model for photometry and spectroscopy. σ^{photo} and σ^{spec} represent the uncertainties on the measured photometry and spectrum. We consider the photometry independent from the spectrum so we combine the likelihoods when jointly model the spectrophotometry:

$$\log \mathcal{L} \approx \log \mathcal{L}^{\text{photo}} + \log \mathcal{L}^{\text{spec}}. \quad (16)$$

$p(\theta)$ is the prior on the SPS parameters. For most of our parameters, we use uninformative uniform priors with conservatively chosen ranges that are listed in Table 3.1. However, for the priors of $\{\beta_1, \beta_2, \beta_3, \beta_4\}$, the NMF coefficients for the SFH, we use a Dirichlet distribution. With a Dirichlet distribution, β_i are within $0 < \beta_i < 1$ and satisfy the constraint $\sum_i \beta_i = 1$. This maintains the normalization of the SFH in Eq. 7.

Now that we can evaluate the posterior at given θ , we derive the posterior distributions using Markov Chain Monte Carlo (MCMC) sampling. We use the Karamanis & Beutler (2020) ensemble slice sampling MCMC algorithm with the ZEUS Python package. Ensemble slice sampling is an extension of standard slice sampling that does not require specifying the initial length scale or any further hand-tuning. Furthermore, it generally converges faster than other MCMC algorithms (*e.g.* Metropolis and standard slice sampling) and generates chains with significantly lower autocorrelation.

When we sample the posterior, we do not directly sample our 12 dimensional SPS parameter space. This is because we impose a Dirichlet prior on the SFH NMF coefficients. Dirichlet distributions are difficult to directly sample so we instead use the Betancourt (2012) sampling method, which transforms an N dimensional Dirichlet distribution into an easier to sample $N - 1$ dimensional space. Hence, we sample the posterior in the transformed 11 dimensional space. Given this dimensionality, we run our MCMC sampling with 30 walkers. Overall, we find that the sampling converges after 2,500 iterations with a 500 iteration burn in. Deriving the posterior distribution from a joint SED modeling of photometry and spectra, with the emulator, takes 0.5 CPU hours. In principle, since our emulator uses a PCA NN, we can further expedite our parameter inference using more efficient sampling methods that exploit gradient information, such as Hamiltonian Monte Carlo. We will explore further expediting our SED modeling in future works.

In Figure 3.1 we present the posterior distribution of our 12 SPS model parameters for an arbitrarily chosen LGAL mock observation. We mark the 68 and 95 percentiles of the distribution with the contours. The posterior distribution reveals there are significant degeneracies between SPS parameters — *e.g.* β_2^{SFH} and f_{burst} . Furthermore, the distribution is multimodal (see f_{burst} panels). With our Bayesian SED modeling, we are able to capture such complexities in the posterior. In the bottom panels, we compare our SPS model evaluated at the best-fit parameters (orange) with the LGAL mock observations (black). On the left, we compare the g, r, z band magnitudes; on the right, we compare the DESI spectroscopy. We find excellent agreement between the best-fit SPS model and mock observations.

TODO

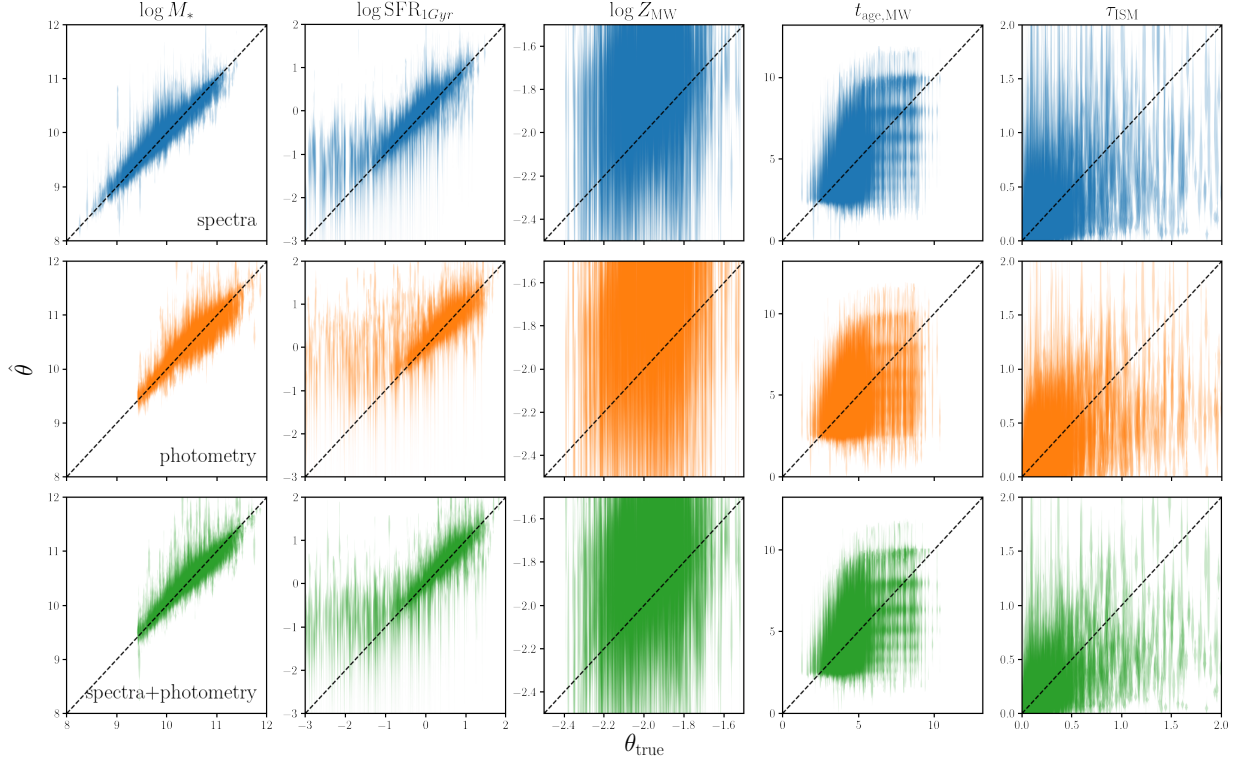


Figure 6. Comparison between the true galaxy properties, θ_{true} , and those inferred from SED modeling of mock observations, $\hat{\theta}$. From the left to right columns, we compare $\log M_*$, $\log \overline{\text{SFR}}_{1\text{Gyr}}$, $\log Z_{\text{MW}}$, $t_{\text{age,MW}}$ and τ_{ISM} . The inferred galaxy properties are derived from SED modeling of mock spectra (top), photometry (middle), and spectrophotometry (bottom). For each simulated galaxy, we represent the marginalized posterior of θ with a violin plot. *The posteriors demonstrate that, overall, we can derive accurate and precise constraints on certain galaxy properties from joint SED modeling of DESI photometry and spectra.*

4. RESULTS

The goal of this work is to demonstrate the precision and accuracy of inferred galaxy properties for PROVABGS. We apply our SED modeling to the mock observables of **100** LGAL galaxies. From the posterior distributions of the SPS parameters, we derive the following physical galaxy properties: stellar mass (M_*), SFR averaged over 1 Gyr ($\overline{\text{SFR}}_{1\text{Gyr}}$), mass-weighted stellar metallicity (Z_{MW}), and diffuse-dust optical depth (τ_{ISM}). M_* and τ_{ISM} are both SPS model parameters. We derive $\overline{\text{SFR}}_{1\text{Gyr}}$ and Z_{MW} as

$$\overline{\text{SFR}}_{1\text{Gyr}} = \frac{\int_{t_{\text{age}}-1\text{Gyr}}^{t_{\text{age}}} \text{SFH}(t) dt}{1\text{Gyr}} \quad \text{and} \quad Z_{\text{MW}} = \frac{\int_0^{t_{\text{age}}} \text{SFH}(t) ZH(t) dt}{M_*}. \quad (17)$$

In Figure 6, we compare the galaxy properties inferred from SED modeling the mock observations, $\hat{\theta}$ to the true (input) galaxy properties, θ_{true} of the simulated galaxies. In each column, we compare $\log M_*$, $\log \overline{\text{SFR}}_{1\text{Gyr}}$, $\log Z_{\text{MW}}$, $t_{\text{age,MW}}$, and τ_{ISM} from left to right. The inferred properties in the top, middle, and bottom rows are derived from SED modeling of spectra, photometry, and

TODO

spectrophotometry, respectively. In each panel, we plot $\hat{\theta}$ using a violin plot, where the width of the marker represents the marginalized posterior distribution of θ . We note that in the comparison with SED modeling spectra only, we do not include f_{fiber} . Therefore, the true stellar mass in this case corresponds to $f_{\text{fiber}} \times M_*$. *Overall, the comparison demonstrates that we can robustly infer galaxy properties using the PROVABGS SED modeling.*

In more detail, we find that we infer unbiased and precise constraints on M_* throughout the entire M_* range. We also infer robust $\overline{\text{SFR}}_{1\text{Gyr}}$ above $\log \overline{\text{SFR}}_{1\text{Gyr}} > -1$ dex; below this limit, however, the inferred $\overline{\text{SFR}}_{1\text{Gyr}}$ are significantly less precise and overestimate the true $\overline{\text{SFR}}_{1\text{Gyr}}$. This bias at low $\overline{\text{SFR}}_{1\text{Gyr}}$ is caused by model priors, which we discuss in further detail later in [Section 5](#) and [Appendix A](#). Both Z_{MW} and $t_{\text{age,MW}}$ are not precisely constrained. However, Figure 6 does not exhibit clear biases in the constraints. For $t_{\text{age,MW}}$, the posteriors reveal the log-spaced t_{lookback} binning used in our SPS model for $t_{\text{age,MW}} > 6$ Gyr. Lastly, τ_{ISM} is overall accurately inferred for galaxies with low τ_{ISM} but appears to be underestimated for high τ_{ISM} .

The overall constraints on galaxy properties for the mock observations is especially encouraging due to the significant differences in the forward model used to generate the observations and the SPS model used in the SED modeling. First, the SFHs in the mock observations are taken directly from LGAL simulation outputs while the SFH parameterization in the SPS model is based on NMF bases fit to IllustrisTNG galaxy SFHs. Second, in the forward model, we construct the SED of the bulge and disk components of the simulated galaxies separately: the components have separate SFHs and ZHs. Lastly, we use different dust prescriptions: [Mathis \(1983\)](#) dust attenuation curve in the forward model and [Kriek & Conroy \(2013\)](#) dust attenuation curve in the SPS model. Despite these significant differences, our constraints on certain galaxy properties are unbiased and precise.

Figure 6, also highlights the advantages of jointly modeling spectra and photometry. Comparing the constraints from spectrophotometry to photometry alone, we find that including spectra significantly tightens the constraints for all properties. In addition to tightening constraints, including spectra also appears to reduce biases of the constraints. For instance, with only photometry, we derive significantly more biased $\overline{\text{SFR}}_{1\text{Gyr}}$ constraints. This is due to the limited constraining power of photometry, which allows the posteriors to be dominated by model priors. Adding spectra, significantly increases the contribution of the likelihood and ameliorates this effect.

Beyond qualitative comparisons of the posterior, we want to quantify the precision and accuracy of the inferred galaxy properties. Let $\Delta_{\theta,i}$ be the discrepancy between the inferred and true parameters for each galaxy: $\Delta_{\theta,i} = \hat{\theta}_i - \theta_i^{\text{true}}$. Then, if we assume that $\Delta_{\theta,i}$ are sampled from a Gaussian distribution,

$$\Delta_{\theta,i} \sim \mathcal{N}(\mu_{\Delta_{\theta}}, \sigma_{\Delta_{\theta}}), \quad (18)$$

the mean ($\mu_{\Delta_{\theta}}$) and standard deviation ($\sigma_{\Delta_{\theta}}$) of the distribution are population hyperparameters that represent the accuracy and precision of the inferred posteriors for the galaxy population. We can derive $\mu_{\Delta_{\theta}}$ and $\sigma_{\Delta_{\theta}}$ using a hierarchical Bayesian framework (*e.g.* [Hogg et al. 2010](#); [Foreman-Mackey et al. 2014](#); [Baronchelli et al. 2020](#)).

Let $\{\mathbf{X}_i\}$ represent the photometry or spectrum of a galaxy population and $\eta_{\Delta} = \{\mu_{\Delta_{\theta}}, \sigma_{\Delta_{\theta}}\}$ be the population hyperparameters. Our goal is to constrain η_{Δ} from $\{\mathbf{X}_i\}$ — *i.e.* $p(\eta_{\Delta} | \{\mathbf{X}_i\})$. As

usual, we can expand

$$p(\eta_\Delta | \{\mathbf{X}_i\}) = \frac{p(\eta_\Delta) p(\{\mathbf{X}_i\} | \eta_\Delta)}{p(\{\mathbf{X}_i\})} \quad (19)$$

$$= \frac{p(\eta_\Delta)}{p(\{\mathbf{X}_i\})} \int p(\{\mathbf{X}_i\} | \{\theta_i\}) p(\{\theta_i\} | \eta_\Delta) d\{\theta_i\}. \quad (20)$$

θ_i is the SPS parameters for galaxy i and $p(\{\mathbf{X}_i\} | \{\theta_i\})$ is likelihood of the set of observations $\{\mathbf{X}_i\}$ given the set of $\{\theta_i\}$. Since the likelihoods for each of the N galaxies, $p(\mathbf{X}_i | \theta_i)$, are not correlated, we can factorize and write the expression above as

$$= \frac{p(\eta_\Delta)}{p(\{\mathbf{X}_i\})} \prod_{i=1}^N \int p(\mathbf{X}_i | \theta_i) p(\theta_i | \eta_\Delta) d\theta_i \quad (21)$$

$$= \frac{p(\eta_\Delta)}{p(\{\mathbf{X}_i\})} \prod_{i=1}^N \int \frac{p(\theta_i | \mathbf{X}_i) p(\mathbf{X}_i)}{p(\theta_i)} p(\theta_i | \eta_\Delta) d\theta_i \quad (22)$$

$$= p(\eta_\Delta) \prod_{i=1}^N \int \frac{p(\theta_i | \mathbf{X}_i) p(\theta_i | \eta_\Delta)}{p(\theta_i)} d\theta_i. \quad (23)$$

$p(\theta_i | \mathbf{X}_i)$ is the posterior for an individual galaxy, so the integral can be estimated using the Monte Carlo samples from the posterior:

$$\approx p(\eta_\Delta) \prod_{i=1}^N \frac{1}{S_i} \sum_{j=1}^{S_i} \frac{p(\theta_{i,j} | \eta_\Delta)}{p(\theta_{i,j})}. \quad (24)$$

S_i is the number of posterior samples and $\theta_{i,j}$ is the j^{th} sample of galaxy i . In practice, $p(\theta_{i,j} | \eta_\Delta) = p(\Delta_{\theta,i,j} | \eta_\Delta)$ is a Gaussian distribution and, hence, easy to evaluate. $p(\theta_{i,j}) = 1$ since we use uninformative and Dirichlet priors (Table 3.1). Lastly, we sample the $p(\eta_\Delta | \{\mathbf{X}_i\})$ distribution using MCMC.

In Figure 7, we present the accuracy (μ_{Δ_θ}) and precision (σ_{Δ_θ}) of our joint SED modeling of spectra and photometry (green) as a function of true galax property. In each panel, we derive $p(\eta_\Delta | \{\mathbf{X}_i\})$ for $\log M_*$, $\overline{\text{SFR}}_{1\text{Gyr}}$, $\log Z_{\text{MW}}$, $t_{\text{age,MW}}$, and τ_{ISM} in bins of widths 0.2 dex, 0.5 dex, 0.05 dex, 0.5 Gyr, and 0.1, respectively. We only include bins with more than three galaxies. μ_{Δ_θ} (solid) and σ_{Δ_θ} (shaded region) are the median values of $p(\mu_{\Delta_\theta}, \sigma_{\Delta_\theta} | \{\mathbf{X}_i\})$ posterior.

For $\log M_*$ we find no significant bias in $\mu_{\Delta_{\log M_*}}$ — we accurately infer the true M_* throughout the entire M_* range. Also, the precision is uniform, $\sigma_{\Delta_{\log M_*}} \sim 0.1$ dex, for all M_* . For $\log \overline{\text{SFR}}_{1\text{Gyr}}$, we accurately infer the true values for $\log \overline{\text{SFR}}_{1\text{Gyr}} > -1$ dex. Below this limit, we significantly overestimate $\log \overline{\text{SFR}}_{1\text{Gyr}}$, consistent with the bias in Figure 6. In fact, we find a $\log \overline{\text{SFR}}_{1\text{Gyr}} \sim -1$ dex lower bound for the inferred $\log \overline{\text{SFR}}_{1\text{Gyr}}$. In terms of precision, we derive tight constraints $\sigma_{\Delta_{\log M_*}} \sim 0.1$ dex from $-1 < \log \overline{\text{SFR}}_{1\text{Gyr}} < 1$ dex but broader constraints $\sigma_{\Delta_{\log M_*}} \sim 0.25 - 0.3$ dex outside this range.

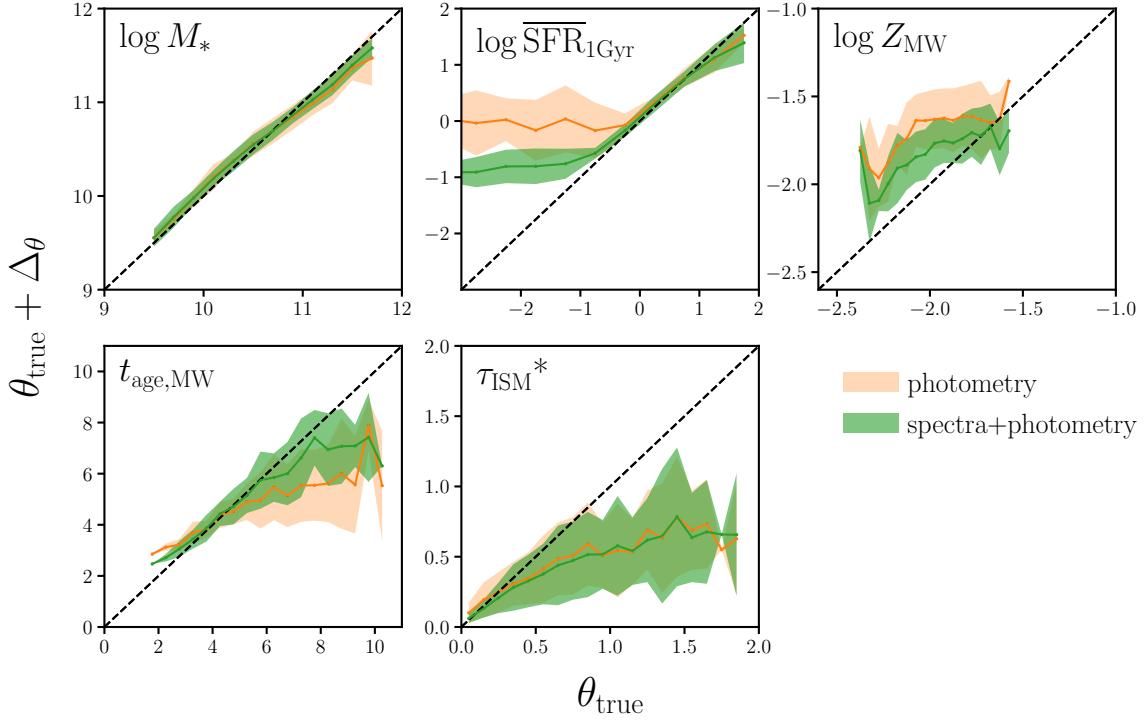


Figure 7. The accuracy and precision of galaxy property posteriors from our joint SED modeling of spectrophotometry, quantified using population hyperparameters $\mu_{\Delta\theta}$ and $\sigma_{\Delta\theta}$, as a function of true galaxy property (green). We plot $\theta_{\text{true}} + \mu_{\Delta\theta}$ in solid line and represent $\sigma_{\Delta\theta}$ with the shaded region. We include $\{\mu_{\Delta\theta}, \sigma_{\Delta\theta}\}$ for SED modeling of photometry alone (orange) for comparison. Including DESI spectra significantly improves both the accuracy and precision of the inferred galaxy properties. $\log \overline{\text{SFR}}_{1\text{Gyr}}$, $\log Z_{\text{MW}}$, and $t_{\text{age,MW}}$ constraints are significantly impacted by well-characterized priors imposed by our SPS model. Meanwhile, discrepancies in the dust prescriptions between our SPS model and the mock observations drive the bias in τ_{ISM} . *Nevertheless, we accurately and precisely infer: $\log M_*$ for all M_* , $\log \overline{\text{SFR}}_{1\text{Gyr}}$ above $\log \overline{\text{SFR}}_{1\text{Gyr}} > -1$ dex, and $t_{\text{age,MW}}$ below 8 Gyr.*

For $\log Z_{\text{MW}}$, Figure 7 reveals a $\log Z_{\text{MW}}$ dependent bias in the inferred values. We overestimate $\log Z_{\text{MW}}$ by ~ 0.2 dex below $\log Z_{\text{MW}} < -1.8$ dex and may underestimate $\log Z_{\text{MW}}$ at the highest Z_{MW} . Meanwhile, $\sigma_{\Delta \log Z_{\text{MW}}} \sim 0.15$ dex is constant throughout the Z_{MW} range, so the bias is small in comparison. For $t_{\text{age,MW}}$, we derive unbiased and precise constraints out to $t_{\text{age,MW}} < 8$ Gyr. For galaxies with older stellar populations, the log-spaced t_{lookback} binning in our SPS model (Section 3.1) expectedly results in underestimated $t_{\text{age,MW}}$ constraints with larger uncertainties ($\sigma_{\Delta t_{\text{age,MW}}} \gtrsim 1$ Gyr). Lastly, for τ_{ISM} we find a significant τ_{ISM} dependence bias in both accuracy and precision. The inferred values increasingly underestimate τ_{ISM} with less precise constraints for greater τ_{ISM} .

The biases in $\overline{\text{SFR}}_{1\text{Gyr}}$, Z_{MW} , $t_{\text{age,MW}}$ are all a consequence of our SPS model priors (Appendix A). $\overline{\text{SFR}}_{1\text{Gyr}}$, Z_{MW} , and $t_{\text{age,MW}}$ are derived quantities; hence, the uniform priors we impose on SPS parameters induce non-uniform priors on them. For our SPS model, we impose a prior on $\log \overline{\text{SSFR}}_{1\text{Gyr}}$ that is skewed and peaks at ~ -10.4 dex (Figure ??). Consequently, the posterior overestimates $\overline{\text{SFR}}_{1\text{Gyr}}$ at low $\overline{\text{SFR}}_{1\text{Gyr}}$. The SPS model also imposes skewed priors on $\log Z_{\text{MW}}$ and $t_{\text{age,MW}}$, which

causes to overestimate $\log Z_{\text{MW}}$ for low Z_{MW} galaxies and underestimate $t_{\text{age,MW}}$ for galaxies with older stellar population.

The bias in our τ_{ISM} constraint is primarily due to intentionally included discrepancies between the SPS model and the mock observations included. First, as we stated earlier, we use a dust prescription with a different attenuation curve in the SPS model than in the forward model. This already places a limit on how accurately we can derive τ_{ISM} ; however, we introduced this discrepancy since we do not know the “true” attenuation curve of observed galaxies in practice. Another reason for the biased τ_{ISM} constraints is that we only attenuate the stellar emission in the disk component of the simulated galaxies and not the bulge component (Section 2.2). The true τ_{ISM} is the optical depth for the disk component while our τ_{ISM} constraints correspond to the optical depth of dust attenuation for the entire galaxies, a quantity that will be lower than the true τ_{ISM} depending on how much the bulge contributes to the SED.

In Figure 7, we also include $\{\mu_{\Delta_\theta}, \sigma_{\Delta_\theta}\}$ for SED modeling of photometry alone (orange) for comparison. We confirm that including spectra significantly tightens the constraints on all of the galaxy properties. **For instance, σ_{Δ_θ} for M_* improves from X to X dex once spectra is included.** In addition to the increased precision, including spectra significantly reduces the bias in the inferred galaxy properties. This is especially clear for $\overline{\text{SFR}}_{1\text{Gyr}}$ below $\log \overline{\text{SFR}}_{1\text{Gyr}} < -1$ dex, where the bias is reduced by ~ 1 dex — an order of magnitude. The overall bias on Z_{MW} is also reduced by ~ 0.3 dex.

TODO

Next, we examine whether the accuracy and precision of our parameter inference is impacted by signal-to-noise ratio (SNR) and photometric color. In Figure 8, we present η_Δ of our joint SED modeling of spectra and photometry as a function of r_{fiber} , r , $g-r$, and $r-z$. r_{fiber} and r magnitudes serve proxies of the SNR for the spectra and photometry, respectively. In each row, we plot η_Δ for a different galaxy property: $\log M_*$, $\overline{\text{SFR}}_{1\text{Gyr}}$, $\log Z_{\text{MW}}$, $t_{\text{age,MW}}$ and τ_{ISM} (from top to bottom). We find no significant dependence on SNR dependence for M_* , $\overline{\text{SFR}}_{1\text{Gyr}}$, $t_{\text{age,MW}}$, or τ_{ISM} . On the other hand, Z_{MW} is significantly overestimated at low spectral SNR (faint $r_{\text{fiber}} > 20$). This highlights that DESI spectra plays a pivotal role in accurately inferring galaxy properties. Hence, when the constraining power from the spectra is reduced, the prior on Z_{MW} dominates the posterior and skews the constraints towards the peak of the prior $\log Z_{\text{MW}} \sim -1.2$.

In terms of $g-r$ and $r-z$ colors, we find a slight color dependence in M_* : $\log M_*$ is marginally underestimated for red galaxies. For $\overline{\text{SFR}}_{1\text{Gyr}}$, there is a more significant color dependence where we overestimate $\log \overline{\text{SFR}}_{1\text{Gyr}}$ by > 0.5 dex for the reddest galaxies ($g-r > 1.5$ and $r-z > 0.6$). The constraints for these galaxies, however, are significantly less precise, $\sigma_{\Delta_{\log \overline{\text{SFR}}_{1\text{Gyr}}}} \sim 0.5$ dex, so they are not as biased as $\mu_{\Delta_{\log \overline{\text{SFR}}_{1\text{Gyr}}}}$ suggests. We also find a significant color dependence in the Z_{MW} constraints, which is primarily driven by the color dependence in the spectral SNR (r_{fiber}). For $t_{\text{age,MW}}$, there is no significant color dependence except at $r-z > 0.6$, where $t_{\text{age,MW}}$ is underestimated. However, this $r-z$ dependence is simply a consequence of $t_{\text{age,MW}}$ being underestimated for $t_{\text{age,MW}} > 8$ Gyr, which was due to the $\log t_{\text{lookback}}$ binning (Figure 7). The simulated galaxies with $r-z > 0.6$ have overall older stellar populations. Lastly, we find no significant color dependence on τ_{ISM} .

5. DISCUSSION

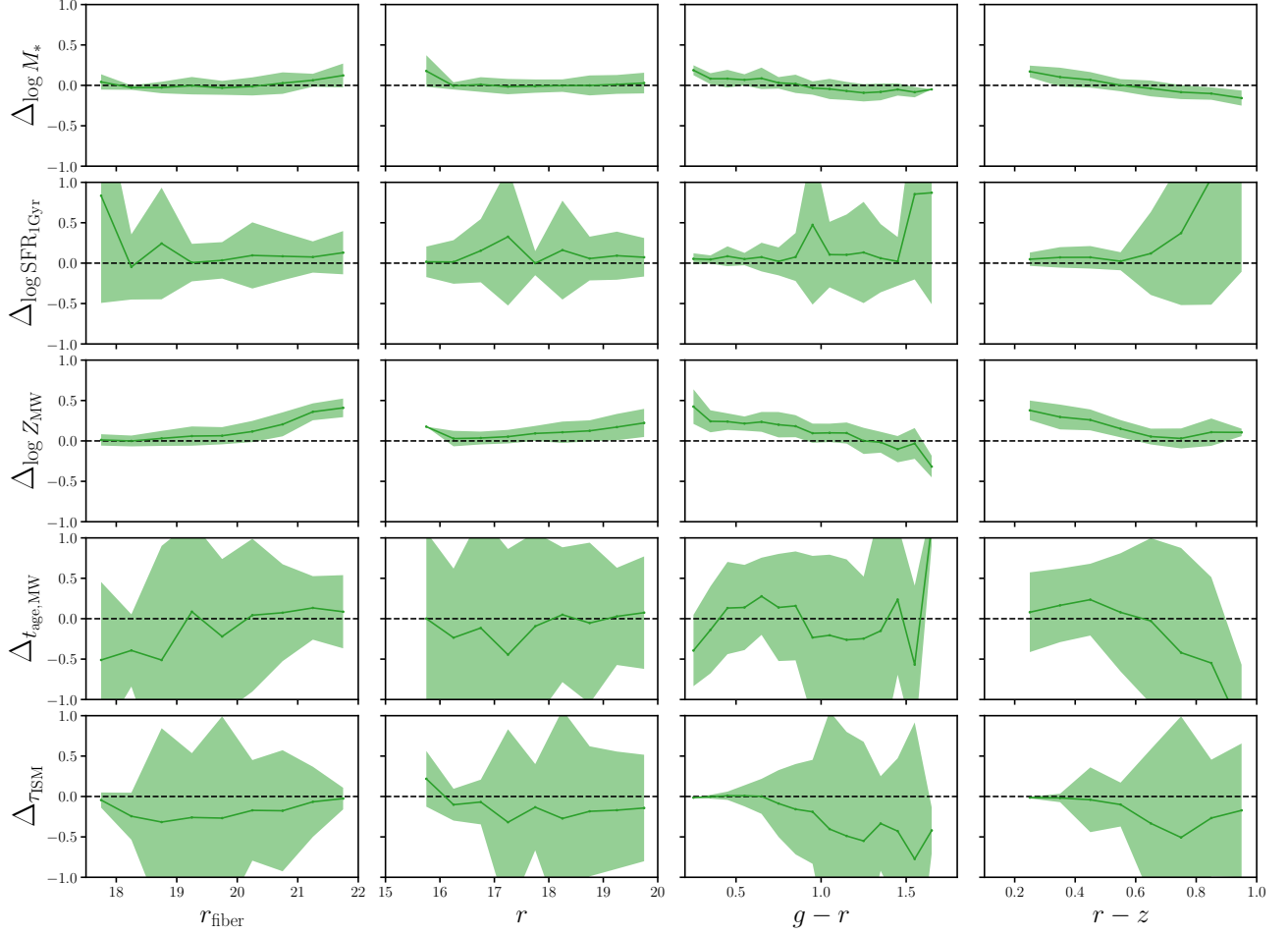


Figure 8. Accuracy and precision of the galaxy properties inferred from joint SED modeling of spectra+photometry as a function of r_{fiber} , r , $g-r$, and $r-z$. From the top to bottom rows, we present η_{Δ} for $\log M_*$, $\log \text{SFR}_{1\text{Gyr}}$, $\log Z_{\text{MW}}$, $t_{\text{age,MW}}$ and τ_{SSM} . r_{fiber} and r magnitudes are proxies for SNR of spectra and photometry. $g-r$ and $r-z$ are the optical photometric colors.

- restatement and discussion of robust galaxy property inference. robustness of most galaxy properties at low SNR, etc.
- reiterate and discuss advantages of spectra+photometry that emphasizes why BGS will be awesome
- Beyond the galaxy properties we discuss in Section 4, we can also derive SFH and ZH
- posterior over MAP
- model priors and preview of how we can correct for it
- caveats: flux calibration — what was implemented versus what will need to be implemented in observations
- caveats: theoretical assumptions — isochrones and stellar libraries, summary of the appendix

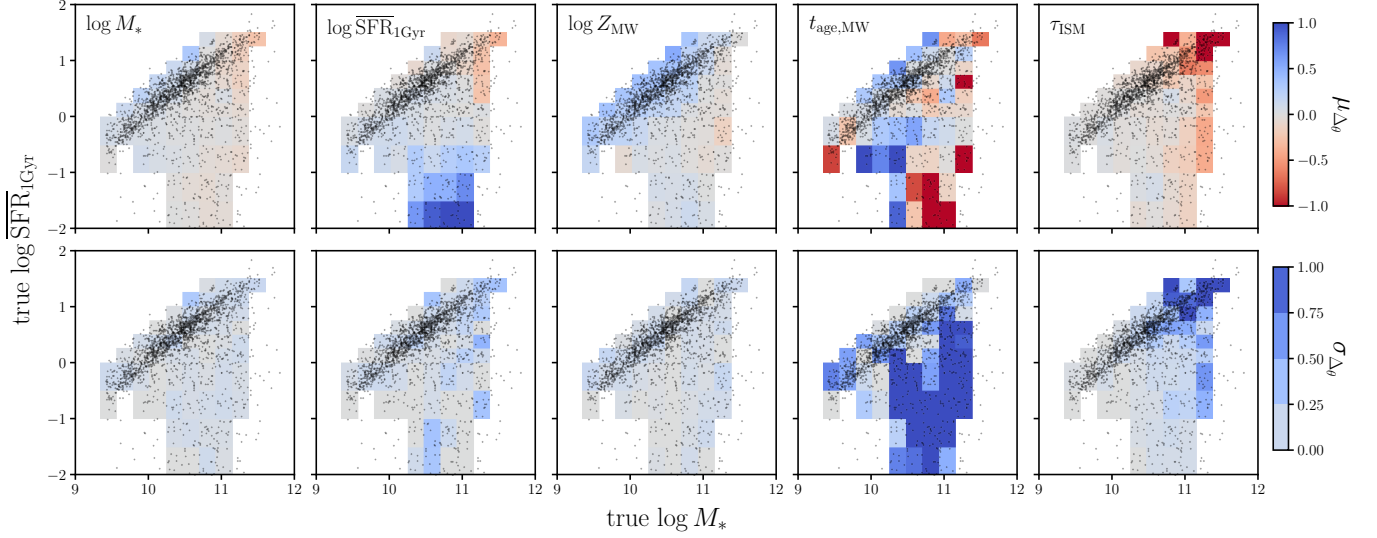


Figure 9. Accuracy and precision of the galaxy properties inferred from joint SED modeling of spectrophotometry as a function of the galaxies’ true M_* and $\overline{\text{SFR}}_{1\text{Gyr}}$. We present $\mu_{\Delta\theta}$ and $\sigma_{\Delta\theta}$ in $(M_*, \overline{\text{SFR}}_{1\text{Gyr}})$ bins for $\log M_*$, $\log \overline{\text{SFR}}_{1\text{Gyr}}$, $\log Z_{\text{MW}}$, $t_{\text{age,MW}}$ and τ_{ISM} in the top and bottom panels respectively.

- despite the caveats, this work demonstrates that the galaxy properties inferred will be robust and awesome. Paragraph that mentions the extension of all the previous science applicatoins
- paragraph that discusses the new science applications with the posteriors.

6. SUMMARY

DESI is great.

Also advertise science papers with specific focus on mock challenge science papers.

ACKNOWLEDGEMENTS

It’s a pleasure to thank Joel Leja, Peter Melchior ... This material is based upon work supported by the U.S. Department of Energy, Office of Science, Office of High Energy Physics, under contract No. DE-AC02-05CH11231. This project used resources of the National Energy Research Scientific Computing Center, a DOE Office of Science User Facility supported by the Office of Science of the U.S. Department of Energy under Contract No. DE-AC02-05CH11231.

APPENDIX

A. SPS MODEL PRIORS

B. SED MODELING UNCERTAINTIES FROM STELLAR EVOLUTION

REFERENCES

- Alsing J., et al., 2019, arXiv:1911.11778 [astro-ph] Baronchelli L., Nandra K., Buchner J., 2020, [Monthly Notices of the Royal Astronomical Society](#), 498, 5284

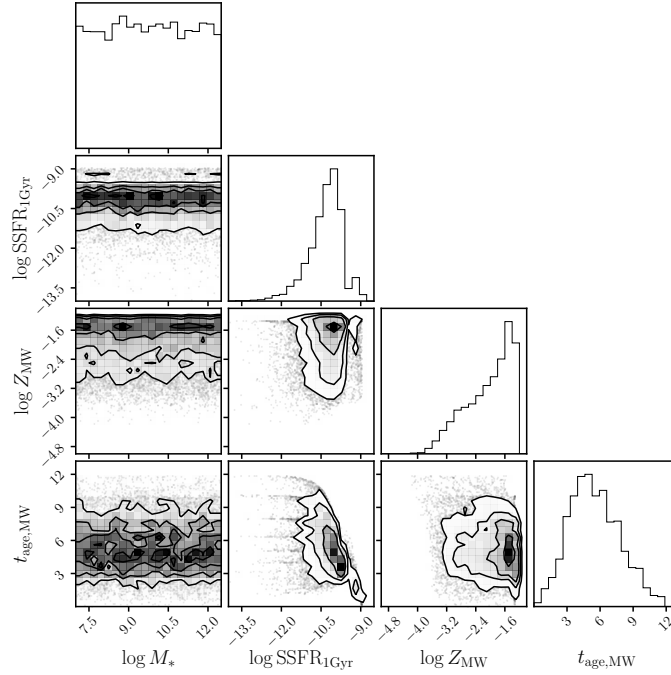


Figure 10. Priors imposed by our SPS model on $\log M_*$, $\log \overline{\text{SSFR}}_{1\text{Gyr}}$, and $\log Z_{\text{MW}}$ at $z = 0.1$.

Betancourt M. J., 2012, [arXiv:1010.3436 \[physics\]](#) 10.1063/1.3703631, pp 157–164

Blanton M. R., et al., 2005, [The Astronomical Journal](#), 129, 2562

Boylan-Kolchin M., Springel V., White S. D. M., Jenkins A., Lemson G., 2009, [Monthly Notices of the Royal Astronomical Society](#), 398, 1150

Caplar N., Tacchella S., 2019, [arXiv:1901.07556 \[astro-ph\]](#)

Carnall A. C., McLure R. J., Dunlop J. S., Davé R., 2017, [arXiv:1712.04452 \[astro-ph\]](#)

Carnall A. C., Leja J., Johnson B. D., McLure R. J., Dunlop J. S., Conroy C., 2018, [arXiv:1811.03635 \[astro-ph\]](#)

Chabrier G., 2003, [Publications of the Astronomical Society of the Pacific](#), 115, 763

Charlot S., Fall S. M., 2000, [The Astrophysical Journal](#), 539, 718

Choi J., Dotter A., Conroy C., Cantiello M., Paxton B., Johnson B. D., 2016, [The Astrophysical Journal](#), 823, 102

Cichocki A., Phan A.-H., 2009, [IEICE Transactions on Fundamentals of Electronics Communications and Computer Sciences](#), 92, 708

Coil A. L., et al., 2011, [The Astrophysical Journal](#), 741, 8

Collaboration P., et al., 2014, [Astronomy & Astrophysics, Volume 571, id.A16](#), pp., 571, A16

Collaboration D., et al., 2016a, [arXiv:1611.00036 \[astro-ph\]](#)

Collaboration D., et al., 2016b, [arXiv:1611.00037 \[astro-ph\]](#)

Conroy C., Gunn J. E., 2010, [The Astrophysical Journal](#), 712, 833

Conroy C., Gunn J. E., White M., 2009, [The Astrophysical Journal](#), 699, 486

Dey A., et al., 2019, [AJ](#), 157, 168

Dotter A., 2016, [The Astrophysical Journal Supplement Series](#), 222, 8

Driver S. P., et al., 2011, [Monthly Notices of the Royal Astronomical Society](#), 413, 971

Févotte C., Idier J., 2011, [arXiv:1010.1763 \[cs\]](#)

Foreman-Mackey D., Hogg D. W., Morton T. D., 2014, [The Astrophysical Journal](#), 795, 64

Hahn C., Tinker J. L., Wetzel A., 2019, [arXiv:1910.01644 \[astro-ph\]](#)

Henriques B. M. B., White S. D. M., Thomas P. A., Angulo R., Guo Q., Lemson G., Springel V., Overzier R., 2015, [Monthly Notices of the Royal Astronomical Society](#), 451, 2663

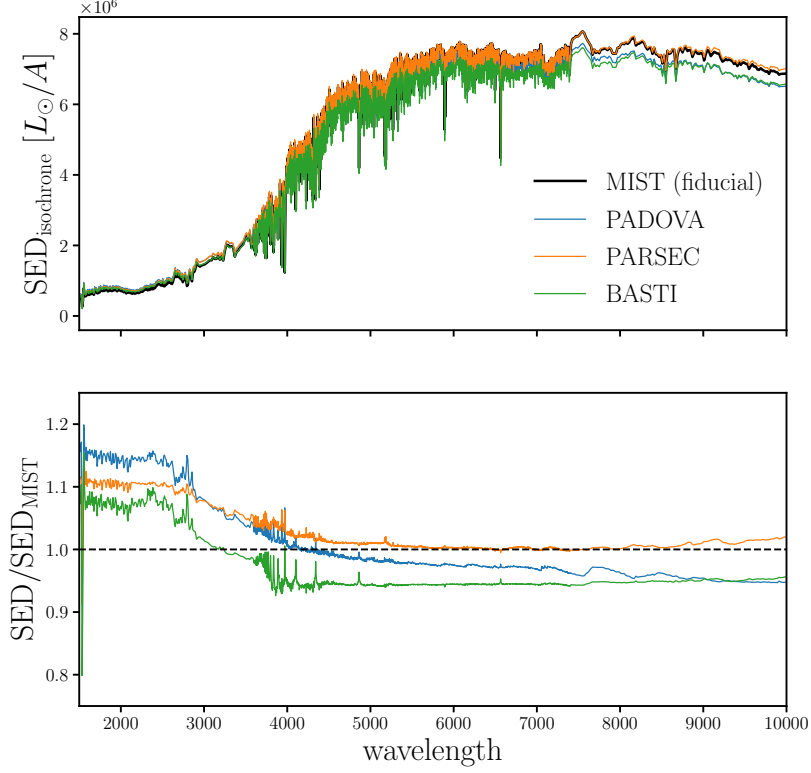


Figure 11. *Top:* Spectral energy distributions generated using MIST (black), Padova (blue), Parsec (orange), and BaSTI (green) isochrone libraries for an arbitrary set of SPS parameters. For our fiducial SED model, we use the MIST isochrone. *Bottom:* Ratios of the SEDs generated using different isochrone libraries over our fiducial MIST SED. The ratios reveal $> 10\%$ discrepancies at rest-frame UV wavelengths and significant offsets at higher wavelengths.

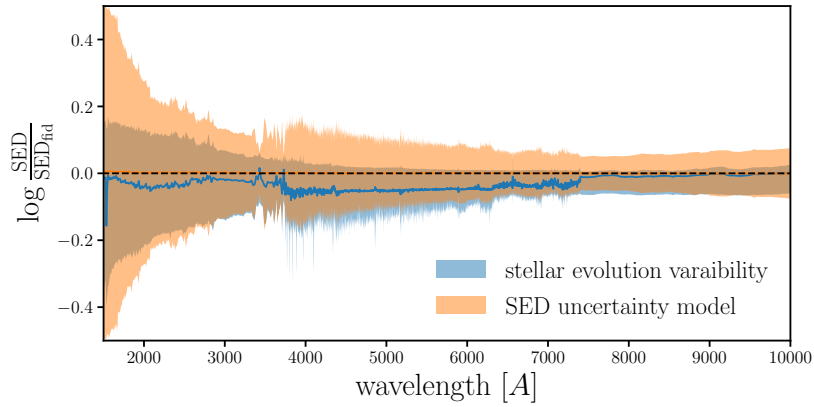


Figure 12.

- Hogg D. W., Myers A. D., Bovy J., 2010, *The Astrophysical Journal*, 725, 2166
- Iyer K. G., et al., 2020, *Monthly Notices of the Royal Astronomical Society*, 498, 430
- Karamanis M., Beutler F., 2020, arXiv e-prints, p. arXiv:2002.06212
- Kriek M., Conroy C., 2013, *The Astrophysical Journal Letters*, 775, L16
- Lee D. D., Seung H. S., 1999, *Nature*, 401, 788
- Leja J., Johnson B. D., Conroy C., van Dokkum P. G., Byler N., 2017, *The Astrophysical Journal*, 837, 170
- Leja J., Carnall A. C., Johnson B. D., Conroy C., Speagle J. S., 2019, *ApJ*, 876, 3
- Mathis J. S., 1983, *The Astrophysical Journal*, 267, 119
- Nelson D., et al., 2018, *Monthly Notices of the Royal Astronomical Society*, 475, 624
- Paxton B., Bildsten L., Dotter A., Herwig F., Lesaffre P., Timmes F., 2011, *The Astrophysical Journal Supplement Series*, 192, 3
- Paxton B., et al., 2013, *The Astrophysical Journal Supplement Series*, 208, 4
- Paxton B., et al., 2015, *The Astrophysical Journal Supplement Series*, 220, 15
- Pillepich A., et al., 2018, *Monthly Notices of the Royal Astronomical Society*, 473, 4077
- Ruiz-Macias O., et al., 2021, *Monthly Notices of the Royal Astronomical Society*, 502, 4328
- Sánchez-Blázquez P., et al., 2006, *Monthly Notices of the Royal Astronomical Society*, 371, 703
- Serra P., Amblard A., Temi P., Burgarella D., Giovannoli E., Buat V., Noll S., Im S., 2011, *The Astrophysical Journal*, 740, 22
- Simha V., Weinberg D. H., Conroy C., Dave R., Fardal M., Katz N., Oppenheimer B. D., 2014, arXiv e-prints, p. arXiv:1404.0402
- Sparre M., Hayward C. C., Feldmann R., Faucher-Giguère C.-A., Muratov A. L., Kereš D., Hopkins P. F., 2017, *Monthly Notices of the Royal Astronomical Society*, 466, 88
- Springel V., et al., 2005, *Nature*, 435, 629
- Springel V., et al., 2018, *Monthly Notices of the Royal Astronomical Society*, 475, 676
- Tacchella S., et al., 2021, arXiv e-prints, 2102, arXiv:2102.12494
- York D. G., et al., 2000, *The Astronomical Journal*, 120, 1579
- Zahid H. J., Geller M. J., Fabricant D. G., Hwang H. S., 2016, *The Astrophysical Journal*, 832, 203